NJC

PAPER

View Article Online
View Journal | View Issue

Cite this: *New J. Chem.*, 2018, **42**, 16115

Supramolecular inter-ionic charge-transfer complexes between derivatives of pyridinium-4-oxime cations and hexacyanoferrate(II) anions†

Blaženka Foretić,‡*[a] Robert Vianello,[b] Dubravka Matković-Čalogović,[c] Dijana Jadreško[d] and Igor Picek‡*[a]

Received 20th June 2018,
Accepted 4th September 2018

DOI: 10.1039/c8nj03066a

rsc.li/njc

Mono- and bis-pyridinium-4-oxime compounds are introduced as new electron acceptors for the formation of colored, supramolecular, inter-ionic charge-transfer complexes with hexacyanoferrate(II) as a donor. The structure and properties of the formed complexes are characterized by a combination of experimental and computational studies. In water, the electron-donor/acceptor dyads exhibit a characteristic charge-transfer band in the visible spectral region whose energy is closely related to the acceptor's electron affinity, LUMO orbital energy and one-electron reduction potential. Such influence of the acceptor's electrochemical nature is revealed through varying the group attached to the N atom of the pyridinium-4-oxime moiety. The color, composition and spectroscopic analysis of the complexes in the solid state provide insights into binding of the cationic and anionic counterparts and the role of lattice water. Crystal structures are reported for two mono-pyridinium-4-oxime/hexacyanoferrate(II) complexes, characterized in solution by UV/Vis and ^{1}H-NMR spectroscopy. Comparison of the solid-state structures and the aqueous-phase dyads reveals the nature of the charge-transfer interactions involving conjugated pyridinium-4-oximes as electron acceptors.

Introduction

Coordination complexes continue to play a central role in the long-standing field of electron transfer chemistry, and their implications for the design of novel systems (*e.g.* molecular electronics and sensor devices) are being intensively pursued in combination with detailed mechanistic studies.[1,2] Oxime ligation has emerged as a powerful tool for the engineering of various types of bioconjugates, which have been successfully used as artificial vectors for drug delivery, imaging probes, synthetic vaccines, and functional arrays.[3] Oximes offer great opportunities in supramolecular chemistry as hydrogen-bond donors/acceptors and in coordination chemistry as metal coordinating ligands.[4,5] When the oxime functionality is combined with an additional coordination site for a metal ion, as in pyridine-oximes, a link is established between coordination complexes and supramolecular assembly. The geometry inherent to such coordination complexes is propagated into low-dimensional architectures *via* intermolecular oxime-oxime hydrogen bonds.[5] Pyridinium oximes are quaternized cationic derivatives of pyridine-oximes in which the pyridine N coordination site for a metal ion is blocked. In such compounds, π-electron delocalization alters the oxime ionization properties, making the compounds more acidic (pK_a values around 7–9). Consequently, many acidic pyridinium oximes, being exceptionally effective nucleophiles, are pharmacologically well-known esterolytic agents used as reactivators of the enzyme acetylcholinesterase initially inhibited by organophosphorus poisons.[6,7] However, these pharmacological compounds possess multiple modes of action, and alternative bioactivities are an active research topic. A particular focus is placed on electron transfer, because useful energetic features are associated with the one-electron reduction product of pyridinium-4-oxime and structurally related compounds.[8] Substantial interdependences between the structure, ionization properties, reactivity and stability in aqueous media have been revealed in the study of carbonyl derivatives of pyridinium-4-oxime.[9,10] The σ-donor and π-acceptor potential of pyridinium-4-oxime

[a] *Department of Chemistry and Biochemistry, School of Medicine, University of Zagreb, Šalata 3, HR-10000 Zagreb, Croatia. E-mail: bforetic@mef.hr, ipicek@mef.hr*
[b] *Division of Organic Chemistry and Biochemistry, Ruđer Bošković Institute, Bijenička 54, HR-10000 Zagreb, Croatia*
[c] *Department of Chemistry, Faculty of Science, University of Zagreb, Horvatovac 102a, HR-10000 Zagreb, Croatia*
[d] *Division for Marine and Environmental Research, Ruđer Bošković Institute, Bijenička 54, HR-10000 Zagreb, Croatia*

† Electronic supplementary information (ESI) available. CCDC 1827974 and 1827975. For ESI and crystallographic data in CIF or other electronic format see DOI: 10.1039/c8nj03066a

‡ Blaženka Foretić and Igor Picek are the main contributors of the article.

derivatives as the sixth ligand in pentacyano(ligand)ferrate(II) complexes, equilibrium and kinetic studies of the aqueous substitution reactions with $[Fe^{II}(CN)_5(H_2O)]^{3-}$ complex, as well as spectroscopic characterization of the isolated solids were reported.[11,12] In the presence of a π-donor, such as the electron-rich metal center in $\{Fe^{II}(CN)_5\}^{3-}$, pyridinium oximes acted as weak π-acceptors resulting in exclusive formation of inner-sphere metal-to-ligand charge-transfer (MLCT) complexes in dilute aqueous solutions. Additionally, because of the affinity of the pyridinium system towards electron, outer-sphere inter-ionic charge-transfer (IICT) associations in solids have been found.[12] For the well-known chromophoric properties of various pyridinium iodide derivatives, which arise from charge-transfer (CT) association, it has been shown that the CT transitions involve an electron transfer (ET) to the pyridinium ring resulting in pyridinyl formation.[13] The role of pyridinium cations in electrochemistry has been believed known for decades, and their radical forms have been proposed as key intermediates in modern photo-electrocatalytic reduction processes.[14] Recently, the formation of organic donor–acceptor systems, including the cyano-pyridine derivative (which functions as an electron acceptor in CT systems) has also been investigated.[15] The presence of weakly coupled donor–acceptor CT states has been detected using their characteristic spectroscopic features, while pyridinium derivatives and pyridinyl species have been discussed as potential redox mediators for the acceleration of net multielectron substrate conversions.[14,15] Evidently, the pyridinium-4-oxime cations have great potential in donor–acceptor CT/ET processes, but to the best of our knowledge, no studies of such an application have yet been reported.

The present study delivers insights into the donor–acceptor complexation between mono- and bis-pyridinium-4-oxime cations (Scheme 1) and hexacyanoferrate(II), $[Fe^{II}(CN)_6]^{4-}$, in aqueous solution and the solid state. The use of the highly charged $[Fe^{II}(CN)_6]^{4-}$ donor, which is inert to substitution, and N-heterocyclic mono- and dications to build IICT complexes has attracted much attention,[16] especially with the 4,4′-dipyridinium dication and its derivatives (viologens).[17] The inter-ionic charge transfer in such systems resembles the intervalence charge transfer of Prussian blue and Prussian blue analogues,[18] important in construction of novel inorganic/organic hybrid polymeric materials. In particular, metal–organic frameworks have been able to unite physical and chemical properties of different organic/inorganic components for many applications, including catalysis, separations, magnetism, sensing and gas storage.[19]

Here we report a combined experimental and computational study of the intricate relationship between the optical and redox properties and supramolecular structure in aqueous solution. Structural characterizations of supramolecular organic–inorganic hybrid crystalline materials are also presented.

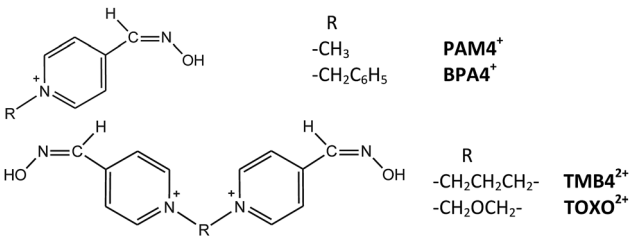

Scheme 1 General structures of investigated electron acceptors.

Results and discussion

IICT complex formation in aqueous solution

When aqueous solutions of $[Fe^{II}(CN)_6]^{4-}$ and the presently-investigated pyridinium-4-oxime were mixed, an immediate reddish violet coloration occurred. These optical properties are reflected in the UV/Vis spectrum, featuring a distinct, broad and low-intensity absorption band with the maximum observed in the visible range as shown in Fig. 1 and Fig. S3 in the ESI.† The band is result of the optical IICT assigned to the $d(t_{2g}^6)p(\pi^0)^* \rightarrow d(t_{2g}^5)p(\pi^1)^*$ electronic transition, *i.e.* from the highest occupied metal-based orbitals of the donor (HOMO) to the lowest unoccupied ligand-based orbitals of the acceptor (LUMO). More specifically this is the optical anion to cation charge-transfer (ACCT) revealing the formation of donor/acceptor compounds in aqueous media. Analogous, new IICT absorption bands were observed when $[Fe^{II}(CN)_6]^{4-}$ was exposed to various other N-heterocyclic acceptors,[16,17a] and comparison of their energies is presented in Table 1. Similar to other optical CT complexes in water, the absorbance of an IICT band decreases with increasing ionic strength, which can be attributed either to the competing equilibria and/or activity coefficient effect.[17a] Nevertheless, at defined pH and ionic strength the predominant formation of donor/acceptor dyads

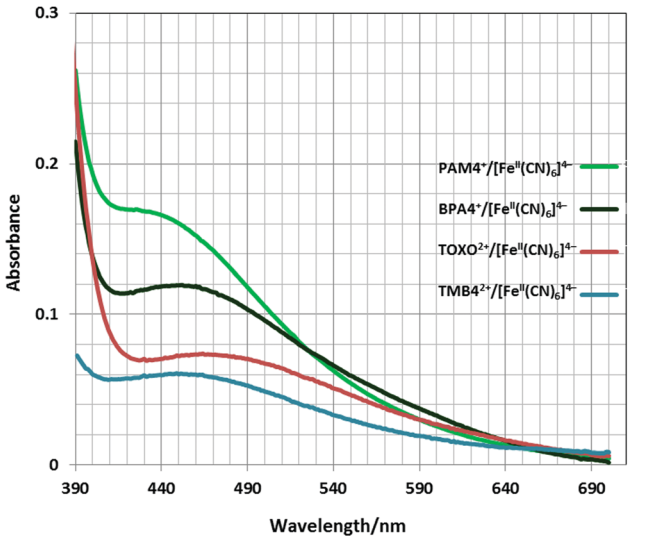

Fig. 1 UV/Vis spectra of the aqueous IICT complexes formed between $[Fe^{II}(CN)_6]^{4-}$ and mono-pyridinium-4-oxime cations ($PAM4^+$ or $BPA4^+$) at a concentration of 12 mM, and bis-pyridinium-4-oxime dications ($TMB4^{2+}$ or $TOXO^{2+}$) at a concentration of 2 mM. pH = 5.65 ± 0.25, t = (25.1 ± 0.1) °C and I = 0.12 M.

Table 1 UV/Vis absorption maxima, optical IICT energies, equilibrium constants K_{ass} (25 °C, I = 0.12 M) and one-electron reduction potentials in water

	$A^{n+}/[Fe^{II}(CN)_6]^{4-}$			
Acceptor, A^{n+}	$\lambda_{max\,CT}$ (nm) $\varepsilon_{max\,CT}$ (M^{-1} cm^{-1})	$E_{max\,CT}$ (eV)	K_{ass} (M^{-1})	E^a (V)
$PAM4^+$	433	2.86	13.6 ± 4.4	−0.84
	133 ± 64			
$BPA4^+$	452	2.74	11.7 ± 4.8	−0.77
	104 ± 31			
$TMB4^{2+}$	459	2.70	28–45[b]	−0.77
	790–920[b]			
$TOXO^{2+}$	478	2.59	45–69[b]	−0.69
	~1000[b]			
MPy^+	~360 sh	3.44	—	−1.50
	—			
MPz^+	470[c]			
N-Methylpyrazinium	150–200	2.64[c]	10–13[c]	−0.65[e]
$MBPy^+$	435[c]			
N-Methyl-4,4′-bipyridinium	150–200	2.85[c]	10–13[c]	−0.90[f]
MV^{2+}	525[d]	2.36[d]	54.2[d]	−0.65[g]
Methyl viologen	690[d]			

[a] E_{pc} or $E_{1/2}$. [b] Estimated values (the low solubility of the IICT complex prevented accurate spectral measurements in solution). [c] Data from ref. 16. [d] Ref. 17*a*. [e] Data from ref. 22. [f] Data for the ligand bound to $\{Fe^{II}(CN)_5\}$ from ref. 23. [g] Data from ref. 24 (−0.446 *vs.* NHE is converted into potential *vs.* Ag/AgCl (3 M KCl)).

can be presented as:

$$A^{n+} + D^{z-} \overset{K_{ass}}{\rightleftharpoons} [A^{n+} : D^{z-} \longleftrightarrow A^{\bullet(n-1)+} - D^{(z+1)-}]$$

electronic ground state

$$\overset{h\nu_{CT}}{\longrightarrow} [A^{n+} : D^{z-} \leftrightarrow A^{\bullet(n-1)+} - D^{(z+1)-}]^*$$

excited state

In general, the resonance hybrid wave function of an IICT complex is composed of an interacting donor and acceptor state that can be described as the sum of all the terms for the A^{n+}:D^{z-} and dative $A^{\bullet(n-1)+}$–$D^{(z+1)-}$ states. The inclusion of the states where an electron has been transferred from D^{z-} to A^{n+} ($A^{\bullet(n-1)+}$–$D^{(z+1)-}$ state) gives rise to partial ground-state charge transfer. The description of these IICT complexes was originally developed by Mulliken and the trend in the optical IICT energies obeys the relationship:[20,21]

$$E_{maxCT} = h\nu_{CT} = I_D - E_A + \Delta \quad (1)$$

In this equation E_{maxCT} is the energy of the IICT band maximum, I_D is the ionization potential of the donor, E_A is the electron affinity of the acceptor and Δ corresponds to the difference between the sums of van der Waals, exchange and repulsion energies of the excited and ground states of the charge transferred, plus the CT resonance energy. For a given donor, as the electron affinity of the acceptor increases, the optical IICT band energy is expected to decrease proportionally. The Mulliken formulation of the CT state energy, written in terms of

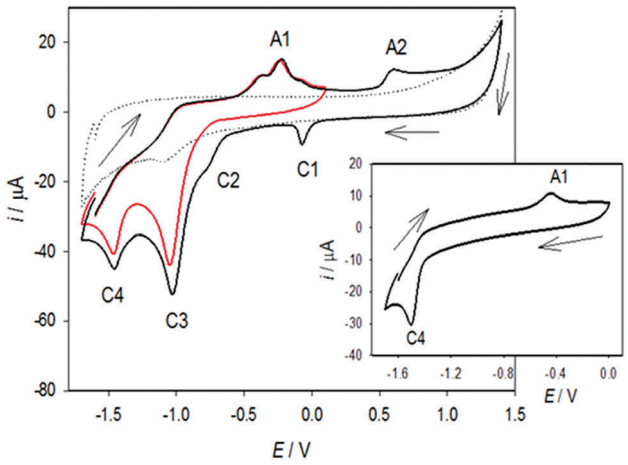

Fig. 2 Cyclic voltammogram (–) of 1 mM BPA4-Cl (and inset: that of 1 mM MPy-I) on glassy carbon electrode in (···) 0.1 M $NaClO_4$. Scan rate, v = 100 mV s^{-1}. Arrows indicate the scan direction.

the donor's I_D and acceptor's E_A, is closely associated with their respective one-electron oxidation and reduction potential. In addition, in simple molecular orbital theory, the HOMO energy is related to the vertical ionization potential of the donor, while the reduction potential of an acceptor is associated with E_A and indicates LUMO energy.

The mono- and bis-pyridinium-4-oxime acceptors, as well as simple *N*-methylpyridinium iodide (MPy-I), were studied by cyclic voltammetry (CV) in water and their relevant electroreduction potentials are presented in Table 1, together with the literature data for selected N-heterocyclic cations for comparison.[22–24] Cyclic voltammograms on a glassy carbon electrode (GCE) in unbuffered 0.1 M $NaClO_4$ aqueous electrolyte at a mean pH value of 5 are shown in Fig. 2 and Fig. S1 in the ESI.† Similar current responses are observed for all the investigated compounds, and the cyclic voltammograms exhibit irreversible behavior typical of pyridinium and oxime-type compounds when using a GCE.[25–28] The irreversible reduction peak at −1.50 V obtained for MPy^+, attributed to the one-electron process resulting in formation of $MPy^{\bullet+}$, is in excellent agreement with the value determined for the pyridinium cation in analogous experimental conditions.[25] In the cyclic voltammogram of BPA4-Cl shown in Fig. 2, two anodic peaks (A1 and A2) and four cathodic peaks (C1–C4) in the potential range from −1.6 V to 1.2 V are seen. To determine the origin of peak C1, another CV experiment was carried out but with the scan direction reversed at 0 V, before the occurrence of peak A2 (see red curve in Fig. 2). As can be seen, only the A1, C3 and C4 peaks are observed, indicating that the peak C1 corresponds to the irreversible reduction (*i.e.* $\Delta E_p = E_{pA2} - E_{pC1} = 0.724$ V) of the hydroxy-nitroso intermediate formed during the initial oxidation of the oxime group. A closely related oxidation manner has been found for the *N*-methylpyridinium-2-oxime in aqueous media.[26] In accordance with the redox behavior of MPy-I itself (see inset in Fig. 2) the highly negative potential (peak C4) results in electroreduction of the parent pyridinium nucleus, while peaks C2 and C3 relate to the consecutive two-electron electroreductions of

oxime and imine moieties. Similar electrochemical properties have been found for pyridine and bis-pyridinium oxime derivatives and a detailed mechanistic insight was provided.[27,28] Specifically, the electroreduction mechanism of the pyridinium-4-imine formation at a given pH involves two successive monoelectronic steps: a fast one-electron transfer to produce the pyridinium-4-oxime radical, which is followed by a slow, rate-determining, second one-electron transfer.[27] Therefore, in this study the electroreduction potential E_{pC2} (peak C2) is taken to represent the one-electron reduction of the investigated pyridinium-4-oxime derivatives into the corresponding pyridinyl radicals (pyridinium-4-oxime^{+}/pyridinium-4-oxime$^{\bullet+}$ or bis-pyridinium-4-oxime^{2+}/pyridinium-4-oxime$^{\bullet 2+}$). The presumed analogy between the electrochemical behavior of the mono- and bis-pyridinium-4-oxime derivatives is justified by the key role of the mono-pyridinium counterparts in symmetric bis-pyridinium compounds. The aqueous reduction potential of these pharmacologically active compounds, which increases significantly at low pH (pH $\sim$ 2), suggests the validity of a one-electron transfer process to rationalize their bioactivities.[8] The CV of $K_4[Fe^{II}(CN)_6]$ in aqueous medium under the same experimental conditions (Fig. S2 in ESI†) revealed quasi-reversible waves, with a peak-to peak separation of *ca.* 0.18 V and midpoint potential of $E_{1/2}[Fe^{III/II}]$ = 0.24 V *vs.* Ag/AgCl (3 M KCl), in agreement with the literature.[29]

The CT character of the electronic transition within the $A^{n+}/[Fe^{II}(CN)_6]^{4-}$ complexes is found to be in accordance with the Mulliken correlation between the one-electron reduction potentials of the acceptors (E_{red}) and the IICT band energies (E_{maxCT}) of the complexes (Fig. 3).

As can be seen from Table 1, introduction of the oxime group to the fourth position of the MPy^{+} ring, to create PAM4^{+}, induces two equal-sized effects: on the one hand increasing the PAM4^{+}/PAM4$^{\bullet+}$ reduction potential (by *ca.* 0.6 V), and on the other hand decreasing the energy of the CT transition (E_{maxCT} by *ca.* 0.6 eV) within the PAM^{+}/$[Fe^{II}(CN)_6]^{4-}$ complex. The electronic effect of the oxime group substantially improves the electron-accepting properties of the conjugated pyridinium-4-oxime system. Additionally, the IICT band energy of the $A^{n+}/[Fe^{II}(CN)_6]^{4-}$ complexes, containing BPA4^{+} and bis-pyridinium-4-oxime acceptors (TMB4^{+}, TOXO^{2+}), decreases, while the reduction potentials of these acceptors themselves increase. These changes are clearly affected by the phenylmethylene group attached to the N atom of the pyridinium-4-oxime moiety and by the oxydimethylene or propylene linkers in the bis-pyridinium acceptors. Furthermore, the subtle differences between the investigated pyridinium-4-oxime acceptors, which form inner-sphere complexes by coordinating with $\{Fe^{II}(CN)_5\}^{3-}$, are clearly reflected in the very intensive MLCT bands[11] in the visible region, whose energies are also linearly dependent on the reduction potential of the corresponding free ligand (see the ESI,† Fig. S4). Therefore, the correlation between the optical ET energies (both, IICT and MLCT) and the electrochemical properties of the respective donor and acceptor ions clearly exist.

For the investigated $A^{n+}/[Fe^{II}(CN)_6]^{4-}$ complexes, the driving force for an ET process can be readily estimated as an endergonic process, with $\Delta G_{ET} = F\cdot(E_{ox} - E_{red})$ ranging from 90 to 168 kJ mol^{-1}. Thus, the electron-transfer rates are prohibitively slow, enabling the spectral observations of transient CT absorptions commonly applicable to electron-donor/acceptor dyads.[30] Consequently, at room temperature, in the electronic ground state of the IICT complexes the presence of a coupled A^{n+}:D^{z-} charge-transfer state rather than $A^{\bullet(n-1)+}$–$D^{(z+1)-}$ electron-transfer state with radical ion-pair character was detected. The equilibrium association constant for $A^{n+}/[Fe^{II}(CN)_6]^{4-}$ complex formation (K_{ass}, M^{-1}) and the molar absorption coefficients (ε_{maxCT}, M^{-1} cm^{-1}) of the IICT-bands were evaluated through analysis of the concentration-dependent intensities of the absorption maximum (Table 1, see Experimental for details). The association constants agree reasonably well with those reported for similar $A^{n+}/[Fe^{II}(CN)_6]^{4-}$ complexes.[16,17a]

Deeper understanding of the relationship between the optical and electrochemical properties was obtained from theoretical calculations. Computational analysis was performed using the M06-2X DFT functional with implicit SMD solvation. The calculated ionization potential, I_P, of 4.05 eV for the $[Fe^{II}(CN)_6]^{4-}$ donor agrees reasonably with the previously published value of 3.50 eV.[17a] The one-electron reduction potentials for the studied pyridinium-4-oxime acceptors obtained by high-level *ab initio* theoretical calculations, along with the electron acceptor affinities, E_A, are presented in Table 2. The calculated values are in accordance with the

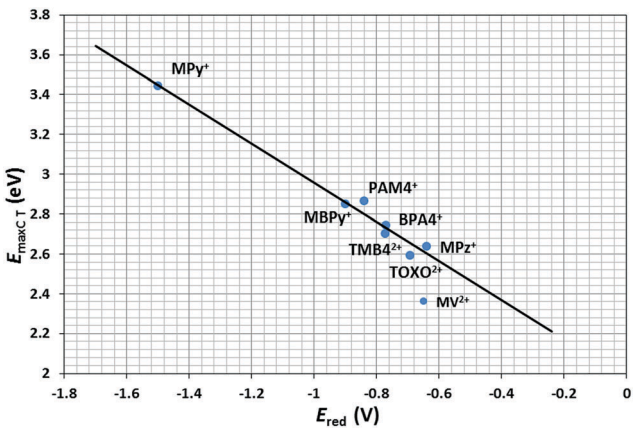

Fig. 3 Mulliken plot for $[Fe^{II}(CN)_6]^{4-}$ complexes with various acceptors, as indicated.

Table 2 Calculated reduction potentials, electron affinities (E_A) and LUMO energies for the pyridinium-4-oxime derivatives

Acceptor, A^{n+}	$E_{calcd\ solution}$ (V)	$-E_A{}^a$ (eV)	$I_P - E_A{}^a$ (eV)	$E(LUMO)^b$ (eV)
PAM4^{+}	−0.98	3.43	0.62	0.74
BPA4^{+}	−0.92	3.49	0.56	0.71
TMB4^{2+}	−0.88	3.53	0.52	0.63
TOXO^{2+}	−0.70	3.71	0.34	0.47

[a] Obtained at the (SMD)/M06-2X/6-311+G(2d,p)/SDD//(SMD)/M06-2X/6-31+G(d)/SDD level of theory. [b] Obtained at the (SMD)/HF/6-311+G(2d,p)/SDD//(SMD)/M06-2X/6-31+G(d)/SDD level of theory.

recently shown rationalization that among the terms contributing the acceptor's reduction potential, even for a series of similar compounds, the difference in the free energy of solvation plays a crucial role for accurately estimating the electron acceptor properties in solution (see the ESI† for details, Table S1).[31] The theoretical one-electron reduction potential for the family of pyridinium-4-oximes are in excellent agreement with the experimental electroreduction potentials E_{pC2} (Table 1), with the largest absolute deviation being 0.15 V for $BPA4^+$. The calculated electron affinities, E_A, (Table 2) for $PAM4^+$ and $BPA4^+$ are very similar, suggesting that the additional benzene moiety in $BPA4^+$ does not significantly affect the ability of these systems to accept an electron. This is further supported by the analysis of the corresponding frontier orbitals (Fig. 4), where it becomes clear that no significant electron density is observed in the additional phenyl ring in the LUMO of $BPA4^+$, while the majority of the electron density is located in the pyridinium-4-oxime moiety, just as in $PAM4^+$. For the bis-pyridinium-4-oxime acceptors, $TMB4^{2+}$ and $TOXO^{2+}$, the corresponding electron affinities are higher, yet only marginally in the former (–3.53 eV), while notably in $TOXO^{2+}$ (–3.71 eV). As expected, the highest electron affinity of $TOXO^{2+}$ is related to the inductive effect of the oxydimethylene linker on the pyridinium-4-oxime system, resulting in its decreased electron density. In addition, the mutual differences among the optical IICT energies are also related to the E_A of the mono- and bis-pyridinium-4-oxime acceptors (Tables 1 and 2).

For the pyridinium-4-oximes studied here, the electron-accepting ability follows the sequence $TOXO^{2+} > TMB4^{2+} \geq BPA4^+ \geq PAM4^+$. An exceptionally good correlation is observed between the acceptors' electron affinities in solution (as well as the matching LUMO orbitals) and the experimentally determined reduction potentials (Table 2). In addition, the optical IICT energies correlate very well with the calculated LUMO energies (see Fig. S4a in the ESI†) and with the calculated $I_P - E_A$ energy difference (Table 2). By comparing the values of $I_P - E_A$, which are in the range of 0.3 to 0.6 eV, with the optical IICT energies, it is obvious that the electrostatic forces are of predominant importance for complex stabilization in solution.

Further insight into the local effects occurring upon formation of the $PAM4^+/[Fe^{II}(CN)_6]^{4-}$ and $BPA4^+/[Fe^{II}(CN)_6]^{4-}$ complexes in D_2O solutions was obtained from ^{1}H-NMR spectroscopy at room temperature. For the 15 mM solution of both complexes, a change in color upon mixing was accompanied by pronounced downfield hydrogen shifts for all pyridinium and alkyl hydrogen atoms (Fig. 5, Fig. S5 and Table S2 in the ESI†). Analogous changes in the ^{1}H-NMR shifts have been found for viologen$^{2+}/[Fe^{II}(CN)_6]^{4-}$ complexes.[17d] The observed deshielding effect is a result of increased polarization of C_{py}–H and C_{alkyl}–H bonds and points to direct hydrogen-bonding interaction with the cyano groups in $[Fe^{II}(CN)_6]^{4-}$. Moreover, increasing the IICT complex concentration (up to 65 mM) resulted in larger downfield shifts, reflecting the stronger attraction between the donor and acceptor because of the

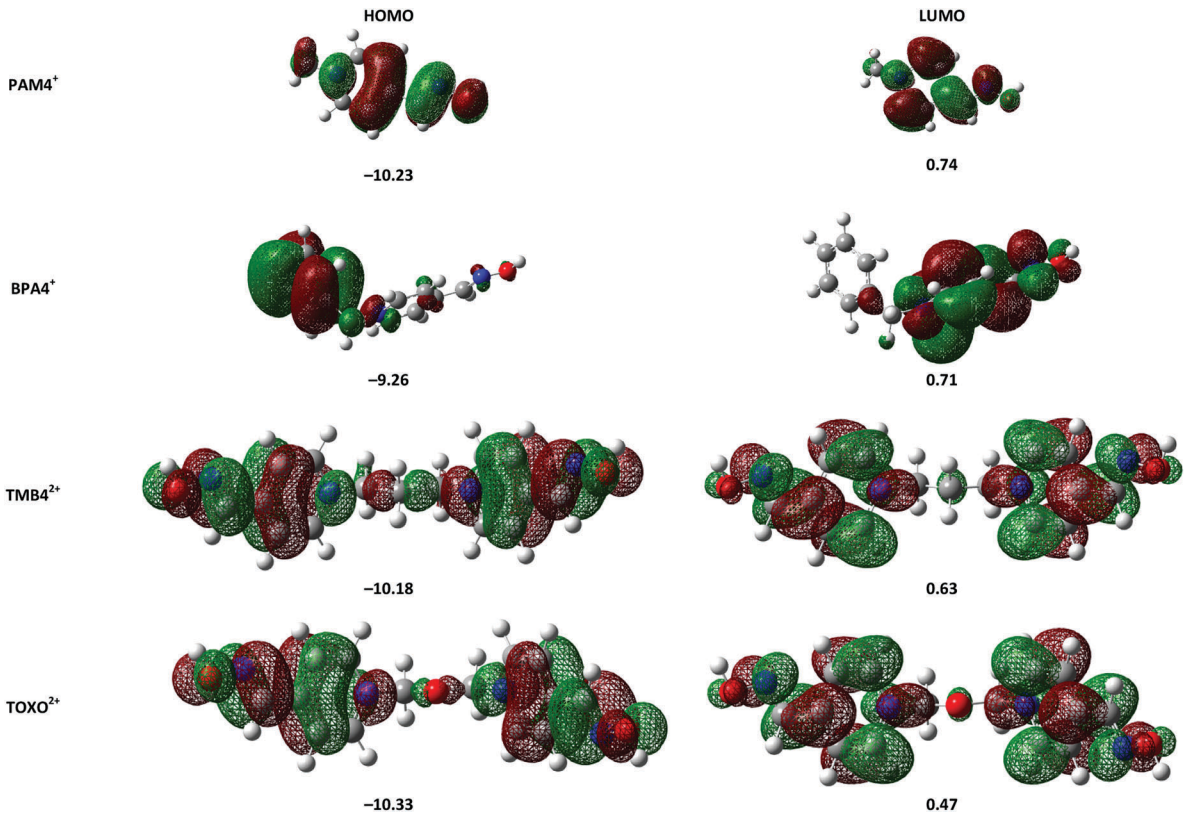

Fig. 4 Representation of HOMO and LUMO orbitals for the pyridinium-4-oxime mono- and dications together with orbital energies (in eV) calculated with the (SMD)/HF/6-311+G(2d,p)//(SMD)/M06-2X/6-31+G(d) level of theory in water.

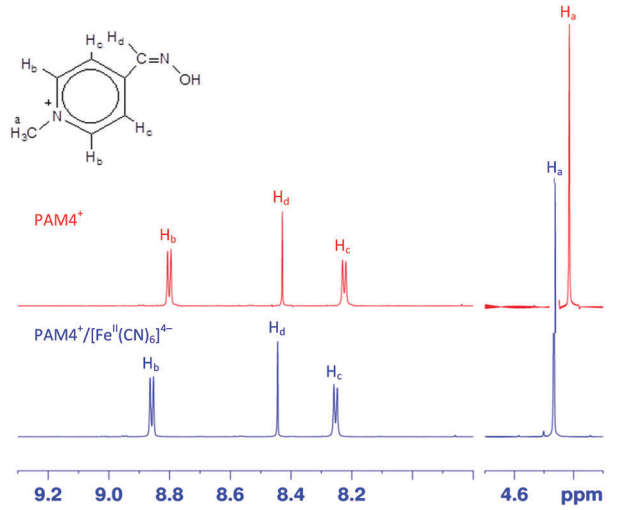

Fig. 5 ^{1}H-NMR spectra of $PAM4^{+}$ (red) and $PAM4^{+}/[Fe^{II}(CN)_6]^{4-}$ (blue) in D_2O at 25 °C; $c(PAM4^{+}) = c([Fe^{II}(CN)_6]^{4-}) = 25$ mM.

exclusion of water molecules from the complex sphere, as was first reported by Haque *et al.*[32a]

This is further rationalized by the substantially small downfield shift of the oxime hydrogen observed in the 15 mM solution, consequence of the strong hydration shell around the highly polar oxime group, which diminishes its direct interaction with the cyano groups in $[Fe^{II}(CN)_6]^{4-}$. The ^{13}C-NMR spectra were measured, with the focus on the cyano carbon atoms. As was previously found for the D_2O solutions of the inner-sphere MLCT pentacyano(pyridinium-4-oxime)ferrate(II) complexes, the significant amount of charge transferred from $\{Fe^{II}(CN)_5\}^{3-}$ to $PAM4^{+}$ or $BPA4^{+}$ induced a notable change in the C≡N bond length, detectible by ^{13}C-NMR as significant upfield shifts of the cyano carbon atoms in comparison with the solution of simple $K_4[Fe^{II}(CN)_6]$.[11,12] In contrast, the association of $[Fe^{II}(CN)_6]^{4-}$ and $PAM4^{+}$ or $BPA4^{+}$ does not lead to any considerable chemical shift ($\Delta\delta \approx 0.08$ ppm), suggesting a low extent of charge transferred and the predominance of an electrostatically-driven donor–acceptor complex. To support this, the model complexes $PAM4^{+}/K_3[Fe^{II}(CN)_6]^{-}$ and $BPA4^{+}/K_3[Fe^{II}(CN)_6]^{-}$ were chosen as the thermodynamically most stable association complexes,[32b] and computationally analyzed using M06-2X with implicit SMD solvation. The calculated electron affinities for $PAM4^{+}$ or $BPA4^{+}$ in these model complexes are only marginally changed relative to the free species. Specifically, the electron affinity of the $PAM4^{+}/K_3[Fe^{II}(CN)_6]^{-}$ complex is –3.39 eV, only a 0.04 eV change relative to $PAM4^{+}$, while for the $BPA4^{+}/K_3[Fe^{II}(CN)_6]^{-}$ complex it is –3.44 eV, representing a change of only 0.05 eV from $BPA4^{+}$. This in turn reveals that the electron density of the respective pyridinium-4-oximes only slightly changes upon complex formation. This also agrees closely with the NBO charge analysis, showing that in the corresponding complexes, the total charge on $PAM4^{+}$ and $BPA4^{+}$ is +1.03 $|e|$. More specifically, only 3% of the overall charge density is perturbed upon association.

Spectroscopic analysis of the supramolecular solids

The freshly isolated supramolecular solids $(PAM4)_6[Fe(CN)_6]I_2$, $(BPA4)_4[Fe(CN)_6]\cdot 10H_2O$, $(TMB4)_2[Fe(CN)_6]\cdot 5H_2O$ and $(TOXO)_2$-$[Fe(CN)_6]$ are poorly soluble in water and exhibit colors which are not composites of the constituents. The association between mono-pyridinium-4-oxime cations and $[Fe^{II}(CN)_6]^{4-}$ resulted in a relatively slow precipitation, allowing the formation of SCXRD-quality crystals. In contrast, the fast precipitation of the complexes between bis-pyridinium-4-oxime dications and $[Fe^{II}(CN)_6]^{4-}$ resulted in microcrystalline powdery solids. We attempted to prepare single crystals by heating the aqueous suspensions. However, thermal degradation of $[Fe^{II}(CN)_6]^{4-}$ led to formation of an insoluble mixture of both an inner-sphere complex formed by bis-pyridinium-4-oxime coordination to the $\{Fe^{II}(CN)_5\}^{3-}$ moiety and an outer-sphere association complex.

All of the isolated solids, like the analogous cyanoiron(II) complexes containing low-spin Fe^{II} with fully occupied t_{2g} levels,[33] produced a single line in ^{57}Fe Mössbauer spectra. The corresponding isomer shift and line width values relative to α-Fe at 298 K were found to range from –0.08 mm s^{-1} to –0.06 mm s^{-1} and from 0.29 mm s^{-1} to 0.32 mm s^{-1}, respectively (Fig. S6 in the ESI†). These values are comparable with those found for $K_4[Fe^{II}(CN)_6]$ itself, without a notable effect of the zeolitic or crystallization water on their ^{57}Fe Mössbauer spectra.[33] In the FTIR spectrum of $K_4[Fe^{II}(CN)_6]\cdot 3H_2O$, characteristic absorption bands for C≡N stretching appeared at 2093 (A_{1g}), 2072 (E_g) and 2045 (F_{1u}) cm^{-1}; for O–H bending in water at 1649 and 1619 cm^{-1}; and for Fe–C bending and Fe–C stretching at 586 and 417 cm^{-1}. All of these were in close agreement with the reported values.[34] The FTIR spectra of the highly hydrated solids showed ν(CN) absorptions characteristic of $[Fe^{II}(CN)_6]^{4-}$ with O_h symmetry, containing two bands: a very strong one at 2042 ± 2 cm^{-1} and a weak one at 2094 ± 3 cm^{-1}. In contrast, in the spectra of the anhydrous or less hydrated (up to $3H_2O$) solids, the ν(CN) was split into at least three absorption bands in the cyanide stretching region (see Fig. S7 in the ESI†). In all of the supramolecular solids an Fe–C bending band was found at 584 ± 2 cm^{-1}. The absorption bands associated with the pyridinium-4-oxime cationic counterparts are practically identical to those reported for the respective pyridinium-4-oxime salts.[11,12] Therefore, within the vibrational time scale at room temperature, the results are consistent with a A^{n+}:D^{z-} trapped formulation of the supramolecular complexes. The same was found for the intervalence-charge-transfer complexes of the $[Ru^{III}(NH_3)_6][Fe^{II}(CN)_5L]$ type (Prussian blue analogues, which contain the electronic state equivalent to $A^{\bullet(n-1)+}$–$D^{(z+1)-}$).[35] The FTIR results are in accordance with the ^{57}Fe Mössbauer study, showing that at room temperature there is no quantifiable degree of ET which would lead to the formation of charge-separated states, such as $[Fe^{III}(CN)_6]^{3-}$ or pyridinyl radicals, in the solid state.

The diffuse reflectance spectra of the supramolecular solids, compared with the corresponding pyridinium-4-oxime salts and $K_4[Fe^{II}(CN)_6]\cdot 3H_2O$, are characterized by a new absorption band in the range of 200 to 1000 nm, with the maximum in the

Table 3 UV/Vis absorption maxima and optical band gap energies of the supramolecular solids

	$\lambda_{max\,CT}$ (nm)	E_g (eV)
$(PAM4)_6[Fe(CN)_6]I_2$	554	1.82
$(BPA4)_4[Fe(CN)_6]\cdot 10H_2O$	563	1.71
$(BPA4)_4[Fe(CN)_6]\cdot 2H_2O$	645	—
$(TMB4)_2[Fe(CN)_6]\cdot 5H_2O$	535	1.82
$(TOXO)_2[Fe(CN)_6]$	548	1.76

Vis spectroscopic region (Table 3, see ESI† for details). From the spectra (see Fig. S8 in the ESI†), the optical band gap energies (E_g) were evaluated and are presented in Table 3. These E_g values are within the typical range of organic semiconductor materials[36] and highlight these supramolecular materials as good candidates for further investigation of photo- and thermally induced charge separation in the solid state.

In addition, the loss of lattice water in $(BPA4)_4[Fe(CN)_6]\cdot 10H_2O$ and formation of the corresponding dihydrate, upon drying the solid under reduced pressure or heating it to 100 °C, results in an irreversible red-brown to deep blue color change, evidenced by a new, very broad and asymmetric band with the maximum at 645 nm. This is presumably indicative of a quantifiable amount of the charge-separated state within the solid complex, as was found for the solid viologen-hexacyanoferrate.[17b] Thus, further studies in the context of both photo- and thermally induced charge separation, by means of EPR, solid-state NMR and *in situ* high-temperature XRD, are in progress.

Crystal structures of the supramolecular complexes

SCXRD analysis of two mono-pyridinium oxime hexacyanoferrate(II) complexes, $(PAM4)_6[Fe^{II}(CN)_6]I_2$ (**1**) and $(BPA4)_4[Fe^{II}(CN)_6]\cdot 10H_2O$ (**2a**), revealed their unique supramolecular networks based on different intermolecular interactions, reflecting the importance of N-substituents on pyridinium-4-oxime. A Cambridge Structural Database (CSD)[37] search for outer-sphere IICT complex structures with the electron donor $[Fe^{II}(CN)_6]^{4-}$ and organic pyridinium derivatives as electron-acceptors revealed only 17 crystal structures. Crystal data and selected bond distances (Å) for **1** and **2a** are given in Tables S4 and S5 in the ESI.† The Fe–C bond lengths are in the range 1.913(2) to 1.927(2) Å in **1** and 1.899(2) to 1.913(2) Å in **2a**, which are consistent with the oxidation state Fe^{II}. For the crystal structures in the CSD containing the $[Fe^{II}(CN)_6]^{4-}$ anion, the Fe^{II}–C bond lengths, solved by the single-crystal diffraction method and refined to an R factor less than 0.075, are in the range 1.886 to 1.947 Å, with a mean value of 1.914(16) Å. The bond lengths of Fe^{III}–C are greater, with the mean value of 1.943(18) Å.

The asymmetric unit in the crystal structure of **1** consists of half of the $[Fe^{II}(CN)_6]^{4-}$ anion (because the Fe^{II} lies at the center of symmetry), one I^- ion and three $PAM4^+$ cations whose atoms are labeled as A, B and C (Fig. 6a and Fig. S9a in the ESI†). Each $[Fe^{II}(CN)_6]^{4-}$ anion is connected to six $PAM4^+$ cations by strong O–H···N_{cyano} hydrogen bonds ranging from 2.610(3) to 2.683(3) Å (Fig. 6a and Table S6 in the ESI†). The $PAM4^+$ cations are connected to cations from the neighboring hexamers by weak

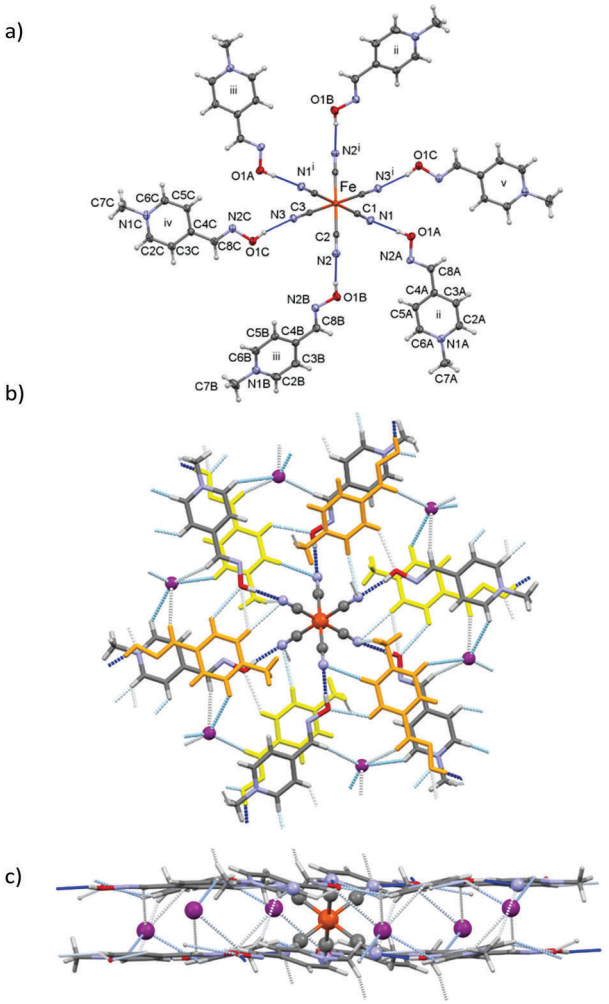

Fig. 6 (a) Drawing of the $[Fe^{II}(CN)_6]^{4-}$ anion and six $PAM4^+$ cations in **1** with the atom labeling scheme (I^- ions are not shown) connected by hydrogen bonds (thin blue lines). Ellipsoids are at the 30% probability level. Symmetry code for cyano ligands: (i) $-x, 1-y, -z$. Symmetry code for $PAM4^+$ cations: (ii) $1-x, 1-y, 1-z$; (iii) $x-1, y, z-1$; (iv) $1-x, -y, -z$; (v) $x-1, 1+y, z$; (b) drawing of the $[Fe^{II}(CN)_6]^{4-}$ anion, six I^- and twelve $PAM4^+$ cations connected by hydrogen bonds shown by dotted lines colored by distance (dark blue for short and light blue for long). $PAM4^+$ cations from neighboring hexamers situated under and above the $PAM4^+$ cations from the given hexamer are shown in yellow and orange, respectively; (c) drawing of one 2D-sandwich iodide layer in **1** with hydrogen bonds shown by dotted lines colored by distance as in (b).

C_{py}–H···N_{cyano} and C_{py}–H···O hydrogen bonds (Fig. 6b). In this way a layered structure is formed, with every other layer containing iodide ions (Fig. 6b), each being an acceptor of five weak C–H···I interactions. Two such 2D-sandwich iodide layers are connected by very weak C_{Met}–H···N_{cyano} hydrogen bonds (Fig. 6c). There are parallel-displaced π–π interactions between the oxime group of one cation and the pyridinium ring of its centrosymmetrically related pair, in such a way that the C8 of one cation lies approximately above the centroid of the pyridinium ring of the other cation. The distances C8···Cg are 3.561(2) Å, 3.531(2) Å and 3.589(2) Å in cations, A, B and C, respectively. The layers in this structure are parallel to (11−1),

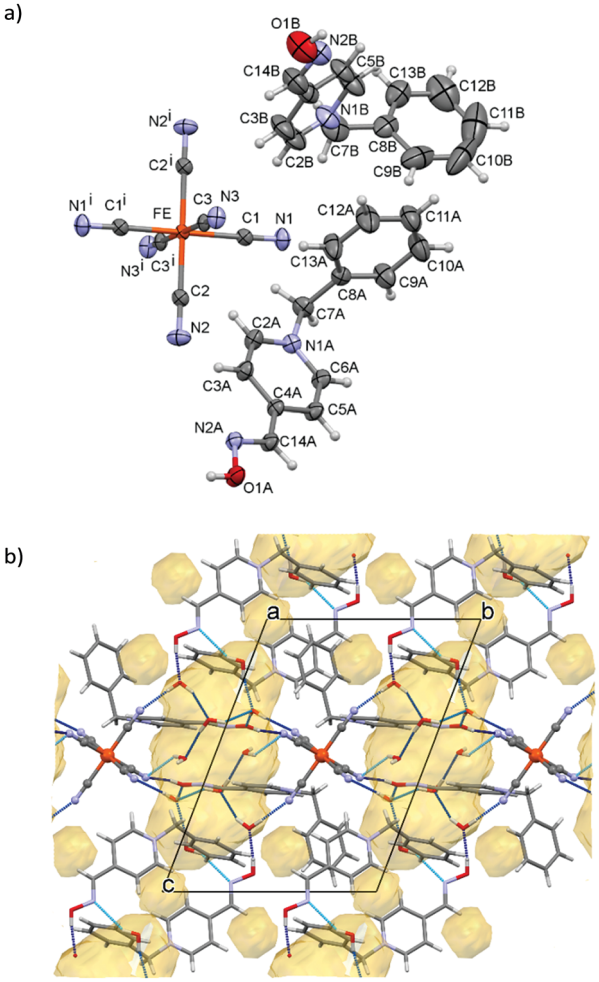

Fig. 7 (a) Drawing of the $[Fe^{II}(CN)_6]^{4-}$ anion and two $BPA4^+$ cations in **2a** with the atom labelling scheme. Ellipsoids are at the 30% probability level. Symmetry code: (i) $-x$, $1-y$, $1-z$; (b) packing of **2a** in the unit cell. Hydrogen bonds interconnecting the cations, anions and water molecules are shown by dotted lines colored by distance (dark blue for short and light blue for long). Voids occupied by water molecules are shown in yellow.

the "top" face of the plate-like crystals, indicating that the crystal growth is slowest in the direction [11−1] (Fig. S10 in the ESI†).

The asymmetric unit of **2a** consists of one half of the $[Fe^{II}(CN)_6]^{4-}$ anion (Fe^{II} lying at the center of symmetry), two $BPA4^+$ cations and five water molecules (Fig. 7a). In the crystal structure the strongest hydrogen bonds are, as in **1**, those involving the hydroxyl groups; however in this structure only $BPA4^+$ (atoms labeled as A) is connected to a cyano ligand (with an O–H···N_{cyano} distance of 2.590(3) Å), while $BPA4^+$ (atoms labeled as B) interacts with a water molecule (with an O–H···O_{water} distance of 2.529(4) Å). Packing of **2a** viewed along the *a*-axis is shown in Fig. 7b. Five hydrogen bonds interconnect the water molecules situated in hydrophilic pockets, three water molecules are bonded to the anion (O–H_{water}···N_{cyano}), and one water molecule to $BPA4^+$ (atoms labeled as B) (O–H_{water}···N_{oxime}), revealing the essential role of water molecules in the supramolecular assembly of this complex (Table S6 in the ESI†). Through this hydrogen bonding network, layers are formed parallel to (001). Both cations also form two weak C–H···N_{cyano} hydrogen bonds. The layers are connected through weak C–H···O_{water} hydrogen bonds and van der Waals interactions into a 3D network. The solvent-accessible area amounts to 16.5% of the unit cell volume but does not form a continuous void (Fig. 7b). Cations $BPA4^+$ show no significant evidence for internal ground-state charge-transfer; the dihedral angles between the phenyl and pyridyl rings in cations A and B amount to 81.92(17)° and 79.57(18)°, respectively. In **2a** the layers are also parallel to the smallest crystal dimension, indicating that the slowest growth is in the [001] direction (Fig. S11 in the ESI†). If left in air, the crystals gradually lose water molecules and cracks appear.

Experimental

Materials

The synthetic procedures for *N*-methylpyridinium-4-oxime iodide (PAM4-I) and *N*-benzylpyridinium-4-oxime chloride monohydrate (BPA4-Cl·H_2O), their spectroscopic characterization (FTIR, FT-Raman, FT-MS, ^{1}H- and ^{13}C-NMR) and crystal structure parameters have been provided in previous studies.[11,12] Potassium hexacyanoferrate(II) trihidrate, $K_4[Fe(CN)_6]\cdot 3H_2O$ (Sigma-Aldrich), *N*-methyl-pyridinium iodide (MPy-I; Sigma-Aldrich), *N*,*N*′-(trimethylene)bis(pyridinium-4-oxime)dibromide (TMB4-2Br; Sigma-Aldrich) and *N*,*N*′-(oxydimethylene)bis(pyridinium-4-oxime)dichloride (TOXO-2Cl, Merck Darmstadt) were used as purchased. The ultra-pure water (ASTM Type 1 quality) obtained using a Millipore Direct-Q 5 purification system was used to prepare solutions.

General physical measurements

The UV/Vis measurements were performed at 25 °C on a Varian Cary Bio 100 and UNICAM UV4 spectrophotometers with thermostated cell holders using 1 cm and 4 cm cuvettes. The ^{1}H and ^{13}C NMR spectra were recorded at room temperature with a Bruker AV-600 spectrometer, operating at 600.13 and 150.9 MHz, respectively. Cyclic voltammograms were recorded using the electrochemical system PGSTAT 101 (Eco-Chemie, Utrecht, Netherlands), controlled by the NOVA 1.5 software and a glassy-carbon electrode of 3.0 mm diameter (MF-2012, Bioanalytical Systems, Inc., West Lafayette, Indiana, USA) as a working electrode. Elemental analysis was performed by using a Perkin Elmer 2400 Series II CHNS elemental analyzer with accuracy percent of +/− 0.3%. The thermogravimetric analysis was performed using a Shimadzu DTG-60H instrument, in the stream of N_2 (50 mL min^{-1}) at a heating rate of 10 °C min^{-1}. The Mössbauer spectra were recorded at 25 °C in the transmission mode using a standard WISSEL GmbH (Starnberg, Germany) instrumental configuration. The ^{57}Co in a rhodium matrix was used as the Mossbauer source. The velocity scale and all the data refer to the metallic α-Fe absorber at 25 °C. Quantitative analyses of the Mossbauer spectra were performed using the MossWin program.[38] Diffuse-reflectance spectra were recorded using Shimadzu UV/Vis-NIR spectrometer (model UV-3600) equipped with an integrated sphere and was calibrated

against the surface of $BaSO_4$ for 100% reflectance (R). Absorption spectra were constructed from diffuse reflectance measurements by expressing the apparent absorbance as $\log(1/R)$. FTIR spectra were recorded on a Perkin Elmer Spectrum GX, Series R spectrometer in the range of 4000–400 cm^{-1} using KBr pellets. A Mettler Toledo pH-meter with an open junction combination polymer electrode was used for pH measurements accurate to ±0.01 pH units.

UV/Vis spectral studies. The stock solutions of the corresponding pyridinium-4-oxime and $[Fe^{II}(CN)_6]^{4-}$ were always freshly prepared. Each reaction mixture was prepared by injecting a stock solution of $[Fe^{II}(CN)_6]^{4-}$ into a thermally equilibrated solution of the corresponding pyridinium-4-oxime contained in a cuvette. The ionic strength was maintained at 0.12 M (NaCl solution was added as needed). The spectrophotometric runs were started immediately. In each reaction mixture, the solutions of corresponding pyridinium-4-oxime and $[Fe^{II}(CN)_6]^{4-}$ were mixed within concentration range of 3.0–12 mM for mono-pyridinium-4-oximes and of 0.5–2.0 mM for bis-pyridinium-4-oximes. For the bis-pyridinium-4-oxime^{2+}/$[Fe^{II}(CN)_6]^{4-}$ complexes, the solubility product is very small, preventing accurate spectral measurements in solution. The $[Fe^{II}(CN)_6]^{4-}$ stock solution was kept in the dark to avoid photochemical degradation and was deaerated with high purity nitrogen continuously bubbled through the system to suppress oxidation of $[Fe^{II}(CN)_6]^{4-}$ to $[Fe^{III}(CN)_6]^{3-}$. The time-dependent spectrum collection have shown that within 10 minutes after reactant mixing the absorption band maximum is exclusively associated with the CT state of the formed IICT complex, which is the only species to have an appreciable absorbance. The equilibrium association constants (K_{ass}/M^{-1}) for the IICT complex formation and corresponding molar absorption coefficients ($\varepsilon_{maxCT}/M^{-1}$ cm^{-1}) at 25 °C and 0.12 M ionic strength have been evaluated by non-linear regression of the experimental data to the following general expression valid for simple 1 : 1 binding:

$$A = \frac{\varepsilon_{maxCT}}{2} \cdot \left\{ \left(c_A + c_D + \frac{1}{K_{ass}} \right) - \sqrt{\left(c_A + c_D + \frac{1}{K_{ass}} \right)^2 - 4 \cdot c_A \cdot c_D \cdot} \right\}$$

where A is absorbance and c_A and c_D refer to the initial concentrations of the acceptor and donor.

NMR studies in solution. The spectra were recorded in D_2O without internal standard present. The ^{1}H-NMR spectra were calibrated by using residual undeuterated solvent as an internal reference (4.80 ppm). A set of reaction mixtures containing different but equal concentrations of $PAM4^+$ or $BPA4^+$ and $[Fe^{II}(CN)_6]^{4-}$ were prepared in D_2O. The concentration range from 15 mM to 65 mM was found to be optimal regarding to the NMR sensitivity restrictions and to avoid precipitation of complexes. Because of these restrictions, the NMR studies of bis-pyridinium-4-oxime^{2+}/$[Fe^{II}(CN)_6]^{4-}$ complex solutions was precluded. The initial solutions of $PAM4^+$ or $BPA4^+$ and $[Fe(CN)_6]^{4-}$ were mixed just before recording the ^{1}H-NMR. To obtain the chemical shift difference, $\Delta\delta$ ($\Delta\delta = \delta_{complex} - \delta_{oxime}$), the solutions of $PAM4^+$ and $BPA4^+$ were also prepared in the same concentration range under same conditions and the ^{1}H-NMR spectra were recorded. The ^{13}C-NMR spectra of 15 mM solutions of both, the free ligands and their complexes were obtained in analogous manner.

Cyclic voltammetric measurements. Successive cyclic voltammograms were recorded in the potential range from –1.60 V to 1.40 V at different scan rates (10 mV s^{-1} to 300 mV s^{-1}). Before each run the glassy-carbon electrode was polished with diamond spray (6 μm), and rinsed with ethanol and deionized water. The platinum rod served as an auxiliary electrode whereas all potentials were given with respect to reference electrode: Ag/AgCl (3 M KCl) with 3 M NaCl in the electrolyte bridge (to prevent formation of sparingly soluble $KClO_4$ in the frit). The 1.0 mM, 6.0 mM and 11.0 mM solutions of mono-pyridinium-4-oximes and 0.76 mM solutions of bis-pyridinium-4-oximes were analyzed at 25 °C. The ionic strength of 0.1 M was adjusted by the addition of analytical grade $NaClO_4$. Before starting each new set of measurements, the solution in the electrolytic cell was deaerated with high purity nitrogen (99.999%) for 15 min. A nitrogen blanket was maintained thereafter.

SCXRD structure determination. Diffraction data were collected from suitable single crystals of **1** and **2a** on an Oxford Diffraction Xcalibur single-crystal diffractometer with Xcalibur Sapphire 3 CCD detector and Mo Kα radiation. The CrysAlis Pro Software system, Version 171.38.43 was used for data collection and reduction.[39] The crystal structures were solved by the direct methods using SHELXS program[40] and refined by the full-matrix least-squares method based on F^2 against all reflections using SHELXL-14 program,[41] both integrated in the WinGX system.[42] All non-hydrogen atoms were refined anisotropically. Hydrogen atoms bound to carbon atoms were placed in calculated positions and refined using the riding model, with $U_{iso(H)}$ values set at $1.2U_{eq}$ of their carbon atom. Hydroxyl hydrogen atoms were refined by using the rotating group refinement (HFIX 147) with $U_{iso(H)}$ values set at $1.5U_{eq}$ of the oxygen atom. Water hydrogen atoms were fixed at O–H of 0.85 Å. Geometry parameters were calculated using PLATON.[43] The structure drawings were prepared using MERCURY.[44] The crystallographic data are summarized in Tables S4 and S5, in the ESI.† The voids occupied by water molecules were calculated by the Hydrate analyzer program in MERCURY (probe radius 1.2 Å).

Computational details. As a good compromise between accuracy and the computational feasibility, all molecular geometries were optimized in the gas-phase by the very efficient M06-2X DFT functional employing the 6-31+G(d) basis set for carbon, nitrogen, oxygen and hydrogen atoms and the Stuttgart–Dresden (SDD) effective core potentials[45] for the inner electrons of iron atoms and its associated double-ζ basis set for the outer ones. Radical species were treated with the unrestricted UM06-2X approach. Thermal Gibbs free energy corrections were extracted from the corresponding frequency calculations without the scaling factors. The final single-point energies were attained with a highly flexible 6-311+G(2d,p) basis set giving rise to the M06-2X/6-311++G(d,p)/SDD//M06-2X/6-31+G(d)/SDD model used here in the gas-phase.

In this way, all thermodynamic values reported in this work correspond to a room temperature of 298.15 K and a normal pressure of 1 atm. To account for the solvation effects, thermodynamic parameters in the aqueous solution were calculated from the corresponding gas-phase values on structures reoptimized with the (SMD)/M062X/6-31+G(d)/SDD model with all parameters corresponding to pure water, and utilizing the experimental value of $\Delta G_{SOLV}(K^+)_{WATER} = -79.4$ kcal mol^{-1}.[46] In this way, the solvation free energies were calculated as a difference between the corresponding SMD and gas-phase calculations at the same level of theory. Atomic charges were obtained by natural bond orbital (NBO) analysis[47] as single-point calculations using the (SMD)/M062X/6-31+G(d)/SDD model in water. All of the calculations were performed using the Gaussian 09 software.[48]

Isolation of the supramolecular materials

(PAM4)$_6$[Fe^{II}(CN)$_6$]I$_2$ (1). To the aqueous solution of $K_4[Fe^{II}(CN)_6]\cdot 3H_2O$ (52.9 mg; 0.125 mmol in 0.5 mL), four-fold excess of PAM4-I solution (133.2 mg; 0.50 mmol in 1.0 mL) was added. The clear reddish-brown mixture was left overnight in the dark at room temperature, yielding SCXRD-quality crystals which were filtered off, washed several times with deionized water and absolute ethanol and then dried in the desiccator under reduced pressure over P_4O_{10} for 24 hours. The mass of the complex was 76 mg (η = 49.3%). Anal. calcd for $C_{48}H_{54}N_{18}O_6FeI_2$: C, 44.74; H, 4.22; N, 19.56 found: C, 44.65; H, 4.35; N, 19.59. FTIR (cm^{-1}): ν(CN)$_{cyano}$, 2057 (vs), 2040 (vs); ν(C=N)$_{oxime}$, 1643 (vs); ν(C–C, C–N)$_{pyridinium\ ring}$, 1612 (m), 1572 (m), 1553 (m), 1520 (s); ν(NO), 1019 (vs), 1002 (vs); δ(Fe–C), 582 (m).

(BPA4)$_4$[Fe^{II}(CN)$_6$]·10H$_2$O (2a). To the aqueous solution of $K_4[Fe^{II}(CN)_6]\cdot 3H_2O$ (31.7 mg; 0.075 mmol in 0.25 mL), a solution of BPA4-Cl·H$_2$O (80.0 mg; 0.30 mmol in 3.75 mL) containing four-fold excess of BPA4$^+$ in respect to $[Fe^{II}(CN)_6]^{4-}$ was added. The clear reddish-brown solution was sealed and left in the dark at room temperature. The violet plate-like SCXRD-quality crystals were extracted directly from a solution. The water content was confirmed by the thermogravimetric analysis in the temperature range 25–125 °C; observed mass loss: 14.13%; calculated mass loss: 14.47% (Fig. S12 in the ESI†). FTIR (cm^{-1}): ν(CN)$_{cyano}$, 2042 (vs); ν(C=N)$_{oxime}$, 1642 (vs); ν(C–C, C–N)$_{pyridinium\ ring}$, 1610 (m), 1519 (m); ν(NO), 1016 (vs, br); δ(Fe–C), 582 (m).

(BPA4)$_4$[Fe^{II}(CN)$_6$]·2H$_2$O (2b). After **2a** was filtered off and washed several times with deionized water and absolute ethanol and then dried in the desiccator under reduced pressure over P_4O_{10} for 24 hours, the irreversible change in color from dark purple to dark blue was perceived. The mass of the final, dark blue material was 34.2 mg (η = 49.8%). Anal. calcd for $C_{58}H_{56}N_{14}O_6Fe$: C, 63.27; H, 5.13; N, 17.81 found: C, 63.02; H, 5.10; N, 17.47. The water content was confirmed by the thermogravimetric analysis in the temperature range 25–110 °C; observed mass loss: 3.21%; calculated mass loss: 3.27% (Fig. S12 in the ESI†). FTIR (cm^{-1}): ν(CN)$_{cyano}$, 2095 (w), 2073 (m), 2043 (s); ν(C=N)$_{oxime}$, 1644 (vs); ν(C–C, C–N)$_{pyridinium\ ring}$, 1610 (m), 1522 (m); ν(NO), 998 (br, vs); δ(Fe–C), 583 (s).

(TMB4)$_2$[Fe^{II}(CN)$_6$]·5H$_2$O. The dark purple complex immediately precipitated at room temperature after addition of TMB4-2Br solution (134.0 mg; 0.30 mmol in 0.5 mL) to the solution of $K_4[Fe^{II}(CN)_6]\cdot 3H_2O$ (63.4 mg; 0.15 mmol in 1.0 mL). The precipitate was filtered off, washed several times with deionized water, absolute ethanol and diethyl ether and then dried in the desiccator under reduced pressure over P_4O_{10} for 24 hours. The mass of the complex was 116.0 mg (η = 88.4%). Anal. calcd for $C_{36}H_{46}N_{14}O_9Fe$: C, 49.43; H, 5.30; N, 22.41 found: C, 48.90; H, 5.28; N, 21.97. The water content was confirmed by the thermogravimetric analysis in the temperature range 25–160 °C; observed mass loss: 10.51%; calculated mass loss: 10.30% (Fig. S12 in the ESI†). FTIR (cm^{-1}): ν(CN)$_{cyano}$, 2041 (vs); ν(C=N)$_{oxime}$, 1644 (vs); ν(C–C, C–N)$_{pyridinium\ ring}$, 1612 (s), 1519 (s); ν(NO), 1014 (vs, br); δ(Fe–C), 582 (m).

(TOXO)$_2$[Fe^{II}(CN)$_6$]. The dark purple product instantaneously precipitated at room temperature by addition of TOXO-2Cl solution (64.7 mg; 0.18 mmol in 0.5 mL) to the solution of $K_4[Fe^{II}(CN)_6]\cdot 3H_2O$ (38.0 mg; 0.09 mmol in 1.0 mL). The precipitate was filtered off, washed several times with deionized water and absolute ethanol and then dried in the desiccator under reduced pressure over P_4O_{10} for 24 hours. The mass of the complex was 58.4 mg (η = 82.3%). Anal. calcd for $C_{34}H_{32}N_{14}O_6Fe$: C, 51.79; H, 4.09; N, 24.87 found: C, 51.13; H, 4.15; N, 24.25. FT-IR (cm^{-1}): ν(CN)$_{cyano}$, 2093 (m), 2073 (s), 2061 (s), 2041 (vs); ν(C=N)$_{oxime}$, 1644 (vs); ν(C–C, C–N)$_{pyridinium\ ring}$, 1608 (vs), 1515 (s); ν(NO), 999 (vs); δ(Fe–C), 585 (s).

Once precipitated from aqueous solution, independently on initial reactant concentrations, complexes could not be re-dissolved in water and in common polar organic solvents such as MeOH, EtOH, acetone and DMSO. Attempts to obtain the SCXRD-quality crystals of the bis-pyridinium-4-oxime^{2+}/$[Fe^{II}(CN)_6]^{4-}$ complexes by slowing down the precipitation at higher temperatures (30 to 40 °C) resulted in thermal decomposition of $[Fe^{II}(CN)_6]^{4-}$ and formation of insoluble mixture of both, inner-sphere complex formed by bis-pyridinium-4-oxime coordination to the $\{Fe^{II}(CN)_5\}^{3-}$ moiety and outer-sphere association complex.

Conclusions

We have investigated the features of the novel ground-state complexes of pyridinium-4-oxime derivatives with hexacyanoferrate(II) in water. The electrochemical and electron-acceptor properties of monocationic and dicationic pyridinium-4-oxime derivatives were studied by a combination of experimental and computational techniques. The existence of weakly coupled donor–acceptor complexes with the characteristic coupled charge-transfer state, rather than an electron-transfer state with radical ion-pair character, was detected. The charge-transfer state energies were found to depend on the acceptor's one-electron reduction potential, its calculated electron affinity and its LUMO orbital energy. Furthermore, we have characterized the supramolecular solids as a new type of organic–inorganic hybrid material. The crystal structures of two complexes were

resolved, yielding valuable insights into the interactions responsible for the supramolecular complex assembly. The interconnected sandwich-like 2D-layers, stabilized by interstitial iodide and parallel-displaced π–π interactions, were found to be a characteristic feature of the anhydrous $PAM_4^+/[Fe^{II}(CN)_6]^{4-}$ supramolecular structure. In contrast, the supramolecular crystal network structure in hydrated $BPA_4^+/[Fe^{II}(CN)_6]^{4-}$ is governed by water molecules incorporated within hydrophilic pockets, essential for the formation of a 3D network. If heated or left in air, the water molecules are lost along with the crystallinity, accompanied by a color change. Further studies of these supramolecular solids, in the context of both photo- and thermally induced charge separation, by means of EPR, solid-state NMR and *in situ* high-temperature XRD, are currently underway. Given the widespread use of pyridinium-4-oxime salts as biologically active and pharmacologically important substances, we believe that assessing the trends and correlations between the optical charge-transfer energies and the electrochemical properties of these π-conjugated acceptors represents an important contribution.

Conflicts of interest

There are no conflicts to declare.

Acknowledgements

We thank M. Jurić for thermal analysis assistance, and the University of Zagreb (grant no. 1118032 and 20282206) and the Croatian Science Foundation (grant no. IP-2014-09-3386) for financial support.

Notes and references

1 See for example: O. S. Wenger, *Chem. Rev.*, 2013, **113**, 3686–3733.
2 See for example: (*a*) A. R. Jose, A. E. Vikraman and K. Girish Kumar, *New J. Chem.*, 2017, **41**, 10828–10834; (*b*) D. Xiang, X. Wang, C. Jia, T. Lee and X. Guo, *Chem. Rev.*, 2016, **116**(7), 4318–4440; (*c*) Y. D. Huang, P. Huo, M. Y. Shao, J. X. Yin, W. C. Shen, Q. Y. Zhu and J. Dai, *Inorg. Chem.*, 2014, **53**, 3480–3487.
3 S. Ulrich, D. Boturyn, A. Marra, O. Renaudet and P. Dumy, *Chem. – Eur. J.*, 2014, **20**, 34–41.
4 (*a*) G. Zhang, B. Ding, L. Chai, Z. Niu, L. Yuan, N. Yan and X. Shi, *Z. Anorg. Allg. Chem.*, 2014, **640**, 2492–2497; (*b*) C. B. Aakeröy, A. S. Sinha, K. N. Epa, P. D. Chopade, M. M. Smith and J. Desper, *Cryst. Growth Des.*, 2013, **13**, 2687–2695.
5 C. B. Aakeröy, A. M. Beatty and D. S. Leinen, *J. Am. Chem. Soc.*, 1998, **120**, 7383–7384.
6 (*a*) N. Singh, Y. Karpichev, B. Gupta, M. L. Satnami, J. Marek, K. Kuca and K. K. Ghosh, *J. Phys. Chem. B*, 2013, **117**(14), 3806–3817; (*b*) F. Mancin, P. Tecilla and U. Tonellato, *Langmuir*, 2000, **16**, 227–233.
7 M. Jokanović, *Curr. Top. Med. Chem.*, 2012, **16**, 1775–1789.
8 P. Kovacic, *Curr. Med. Chem.*, 2003, **10**, 2705–2709.
9 B. Foretić, I. Picek, V. Damjanović, D. Cvijanović and D. Milić, *J. Mol. Struct.*, 2012, **1019**, 196–205.
10 I. Picek, R. Vianello, P. Šket, J. Plavec and B. Foretić, *J. Org. Chem.*, 2015, **80**, 2165–2173.
11 B. Foretić, I. Picek, V. Damjanović, D. Cvijanović, I. Pulić, B. M. Kukovec and D. Matković-Čalogović, *Polyhedron*, 2013, **52**, 733–742.
12 B. Foretić, I. Picek, I. Đilović and N. Burger, *Inorg. Chim. Acta*, 2010, **363**, 1425–1434.
13 R. A. Mackay and E. J. Poziomek, *J. Am. Chem. Soc.*, 1972, **94**, 4167–4170.
14 See for example: (*a*) A. G. Peroff, E. Weitz and R. P. Van Duyne, *Phys. Chem. Chem. Phys.*, 2016, **18**, 1578–1586; (*b*) J. A. Keith and E. A. Carter, *J. Am. Chem. Soc.*, 2012, **134**, 7580–7583.
15 E. Wöß, U. Monkowius and G. Knör, *Chem. – Eur. J.*, 2013, **19**, 1489–1495.
16 H. E. Toma, *Can. J. Chem.*, 1979, **57**, 2079–2084.
17 (*a*) P. M. S. Monk, N. M. Hodgkinson and R. D. Partridge, *Dyes Pigm.*, 1999, **43**, 241–251; (*b*) A. S. Abouelwafa, V. Mereacre, T. S. Balaban, C. E. Ansonb and A. K. Powell, *CrystEngComm*, 2010, **12**, 94–99; (*c*) A. S. Abouelwafa, A. Hauser, V. Mereacre, Y. Lan, G. J. Long, F. Grandjean, G. Buth, C. E. Anson and A. K. Powell, *Inorg. Chem.*, 2017, **56**, 6477–6488; (*d*) R. Papadakis, I. Deligkiozi, M. Giorgi, B. Faured and A. Tsolomitis, *RSC Adv.*, 2016, **6**, 575–585.
18 A. Paolella, C. Faure, V. Timoshevskii, S. Marras, G. Bertoni, A. Guerfi, A. Vijh, M. Armande and K. Zaghib, *J. Mater. Chem. A*, 2017, **5**, 18919–18932.
19 P. Wang, V. M. Zamarion, W. Y. Hamad and M. J. MacLachlan, *Dalton Trans.*, 2015, **44**, 14724–14731.
20 R. S. Mulliken, *J. Am. Chem. Soc.*, 1952, **74**, 811–824.
21 C. J. Bender, *Chem. Soc. Rev.*, 1986, **15**, 475–502.
22 B. J. Coe, S. P. Foxon, E. C. Harper, J. Raftery, R. Shaw, C. A. Swanson, I. Asselberghs, K. Clays, B. S. Brunschwig and A. G. Fitch, *Inorg. Chem.*, 2009, **48**, 1370–1379.
23 B. J. Coe, J. L. Harries, M. Helliwell, L. A. Jones, I. Asselberghs, K. Clays, B. S. Brunschwig, J. A. Harris, J. Garin and J. Orduna, *J. Am. Chem. Soc.*, 2006, **128**, 12192–12204.
24 C. L. Bird and A. T. Kuhn, *Chem. Soc. Rev.*, 1981, **10**, 49–92.
25 E. Lebegue, J. Agullo, M. Morin and D. Belanger, *ChemElectroChem*, 2014, **1**, 1013–1016.
26 (*a*) Q. Zheng, Y. Chen, K. Fan, J. Wu and Y. Ying, *Anal. Chim. Acta*, 2017, **982**, 78–83; (*b*) S. Issac and K. G. Kumar, *Anal. Methods*, 2010, **2**, 1484–1489.
27 A. J. Roman, J. M. Sevilla, T. Pineda and M. Blazquez, *J. Electroanal. Chem.*, 1996, **410**, 15–20.
28 Š. Komorsky-Lovrić, *J. Electroanal. Chem.*, 1990, **289**, 161–169.
29 See for example: C. E. Hotchen, I. J. Maybury, G. W. Nelson, J. S. Foord, P. Holdway and F. Marken, *Phys. Chem. Chem. Phys.*, 2015, **17**, 11260–11268.
30 D. Sun, S. V. Rosokha and J. K. Kochi, *J. Phys. Chem. B*, 2007, **111**, 6655–6666.

31 J. Calbo, R. Viruela, E. Orti and J. Arago, *ChemPhysChem*, 2016, **17**, 3881–3890.
32 (*a*) R. Haque, W. R. Coshow and L. F. Johnson, *J. Am. Chem. Soc.*, 1969, **91**, 3822–3827; (*b*) A. O. Tirler, I. Persson, T. S. Hofer and B. M. Rode, *Inorg. Chem.*, 2015, **54**, 10335–10341.
33 E. Reguera and J. Fernández-Bertráin, *Hyperfine Interact.*, 1994, **88**, 49–58.
34 K. Nakamoto, *Infrared and Raman Spectra of Inorganic and Coordination Compounds, fifth, vol. B: Applications in Coordination, Organometallic and Bioinorganic Chemistry*, John Wiley & Sons Inc., New York, 1997.
35 H. E. Toma, *J. Chem. Soc., Dalton Trans.*, 1980, 471–475.
36 A. Köhler and H. Bässler, *Electronic processes in organic semiconductors*, Wiley-VCH Verlag GmbH & Co., 2015.
37 The Cambridge Structural Database C. R. Groom, I. J. Bruno, M. P. Lightfoot and S. C. Ward, *Acta Crystallogr.*, 2016, **B72**, 171–179.
38 Z. Klencsar, E. Kuzmann and A. Vertes, *J. Radioanal. Nucl. Chem.*, 1996, **201**, 105–118.
39 Rigaku Oxford Diffraction (2016), Rigaku Corporation, Tokyo, Japan.
40 G. M. Sheldrick, *Acta Crystallogr.*, 2008, **A64**, 112–122.
41 G. M. Sheldrick, *Acta Crystallogr.*, 2015, **C71**, 3–8.
42 L. J. Farrugia, *J. Appl. Crystallogr.*, 2012, **45**, 849–854.
43 A. L. Spek, *Acta Crystallogr.*, 2009, **D65**, 148–155.
44 C. F. Macrae, I. J. Bruno, J. A. Chisholm, P. R. Edgington, P. McCabe, E. Pidcock, L. Rodriguez-Monge, R. Taylor, J. van de Streek and P. A. Wood, *J. Appl. Crystallogr.*, 2008, **41**, 466–470.
45 D. Andrae, U. Häussermann, M. Dolg, H. Stoll and H. Preuss, *Theor. Chim. Acta*, 1990, **77**, 123–141.
46 R. G. Lamoureux and B. Roux, *J. Phys. Chem. B*, 2006, **110**, 3308–3322.
47 R. J. P. Foster and F. Weinhold, *J. Am. Chem. Soc.*, 1980, **102**, 7211–7218.
48 M. J. Frisch, G. W. Trucks, H. B. Schlegel, G. E. Scuseria, M. A. Robb, J. R. Cheeseman, G. Scalmani, V. Barone, B. Mennucci, G. A. Petersson, H. Nakatsuji, M. Caricato, X. Li, H. P. Hratchian, A. F. Izmaylov, J. Bloino, G. Zheng, J. L. Sonnenberg, M. Hada, M. Ehara, K. Toyota, R. Fukuda, J. Hasegawa, M. Ishida, T. Nakajima, Y. Honda, O. Kitao, H. Nakai, T. Vreven, J. A. Montgomery, Jr., J. E. Peralta, F. Ogliaro, M. Bearpark, J. J. Heyd, E. Brothers, K. N. Kudin, V. N. Staroverov, R. Kobayashi, J. Normand, K. Raghavachari, A. Rendell, J. C. Burant, S. S. Iyengar, J. Tomasi, M. Cossi, N. Rega, J. M. Millam, M. Klene, J. E. Knox, J. B. Cross, V. Bakken, C. Adamo, J. Jaramillo, R. Gomperts, R. E. Stratmann, O. Yazyev, A. J. Austin, R. Cammi, C. Pomelli, J. W. Ochterski, R. L. Martin, K. Morokuma, V. G. Zakrzewski, G. A. Voth, P. Salvador, J. J. Dannenberg, S. Dapprich, A. D. Daniels, Ö. Farkas, J. B. Foresman, J. V. Ortiz, J. Cioslowski and D. J. Fox, *Gaussian 09, Revision A.02*, Gaussian, Inc., Wallingford, CT, 2009.

